

Supplementary Material for:

Stabilizing Lithium and Sodium Fast-Ion Conduction in Solid Polyhedral-Borate Salts at Device-Relevant Temperatures

Wan Si Tang,^{a,b} Motoaki Matsuo,^c Hui Wu,^a Vitalie Stavila,^d Atsushi Unemoto,^e Shin-ichi Orimo,^{c,e} and Terrence J. Udovic^a

^a *NIST Center for Neutron Research, National Institute of Standards and Technology, Gaithersburg, MD 20899-6102, United States*

^b *Department of Materials Science and Engineering, University of Maryland, College Park, MD 20742-2115, United States*

^c *Institute for Materials Research, Tohoku University, Sendai 980-8577, Japan*

^d *Energy Nanomaterials, Sandia National Laboratories, Livermore, CA 94551, United States*

^e *WPI-Advanced Institute for Materials Research, Tohoku University, Sendai 980-8577, Japan*

The purpose of this communication is to demonstrate the proof of concept that, in general, ball-milling these large-anion *closo*-borate type salts leads to the room-*T* (and lower-*T*) stabilization of their high-*T* disordered phases, enabling enhanced conductivities at more device-relevant temperatures. Na₂B₁₂H₁₂ was used as an appropriate example in Figs. 1-3 since the differing XRD patterns of its ordered monoclinic and disordered pseudo-bcc phases are more easily distinguished from each other than the ordered- and disordered-phase patterns of the other materials studied. Yet, as is shown by the XRD results below, the stabilization of disordered high-*T*-like phases by ball-milling is indicated by Rietveld refinements for all the other materials studied (and at least suggested for Li₂B₁₀H₁₀, since its high-*T* structure is still unknown). It should be noted that we did not attempt to optimize the ball-milling process to maximize the formation of the disordered phases. Fig. 3 demonstrates that both ball-milled and pristine Na₂B₁₂H₁₂ have similar superionic conductivities above the pristine *T*_{trans}. Clearly, more aggressive milling conditions will enhance the disordered-phase fractions and lead to further conductivity improvements below the pristine *T*_{trans}, as demonstrated in Fig. S13. This optimization will be the goal of much more extensive future investigations. Moreover, except for some preliminary experiments with Li₂B₁₂H₁₂ and Na₂B₁₂H₁₂ reported in this communication, we did not undertake detailed thermal aging studies of the different materials to determine their relative resistances to reversion back to “pristine” structural behavior via sintering. The exemplary Li₂B₁₂H₁₂ and Na₂B₁₂H₁₂ results presented in this communication suggest that the sodium salts may be more morphologically robust compared to their lithium congeners, but more extensive experiments (beyond the scope of this study) are necessary to test this hypothesis.

Ball-Milling Treatments

Table S1. The ball-milling treatment conditions for the various samples investigated.

Sample	Cycle Duration (min)		Total time (h)	Total milling time (h)
	BM	Pause		
Na ₂ ¹¹ B ₁₂ H ₁₂	48	12	90	72
NaCB ₁₁ H ₁₂	30	5	100	86
Na ₂ B ₁₀ H ₁₀	50	2	83	80
Li ₂ B ₁₂ H ₁₂	2	0.5	20, 100	16, 80
LiCB ₁₁ H ₁₂	30	5	100	86
Li ₂ B ₁₀ H ₁₀	48	12	100	80
Na ₂ B ₁₀ H ₁₀ :Na ₂ CO ₃ (1:1)	2	0.5	35	28
Na ₂ B ₁₂ H ₁₂ /Na ₂ B ₁₀ H ₁₀ (1:1)	2	0.5	4	3.2

X-ray Powder Diffraction (XRD) Measurements

XRD patterns for the ball-milled materials all display line broadening compared to the pristine materials. Average crystallite sizes (absent any other line-broadening effects such as inhomogeneous strains and lattice imperfections) mentioned below were estimated from the Scherrer equation [1], $t \approx K\lambda/[\beta\cos(\vartheta)]$, where t is the crystallite size (nm), K is the shape factor (rad, assumed to be 0.9), λ is the x-ray wavelength (0.15418 nm), β is the fwhm line broadening of the peak (rad), and ϑ is the Bragg angle (rad). As there is probably a very broad distribution crystallite coherency lengths, this should be considered as only a rough qualitative comparison of relative average crystallite sizes before and after ball-milling.

For the Na₂B₁₂H₁₂ XRD data in Fig. 1, the patterns were refined using the low- T monoclinic $P2_1/n$ and high- T pseudo-bcc $Pm-3n$ structures [2,3]. The refined unit cell parameters for the pristine sample are $a = 7.0240(3)$ Å, $b = 10.6426(5)$ Å, $c = 7.0119(5)$ Å, $\beta = 94.842(4)^\circ$, and $V = 522.29(5)$ Å³ for the low- T structure ($R_p = 0.152$; $R_{wp} = 0.170$). The refined unit cell parameters for the ball-milled sample are $a = 6.981(2)$ Å, $b = 10.672(3)$ Å, $c = 7.009(3)$ Å, $\beta = 94.40(2)^\circ$, and $V = 520.7(3)$ Å³ for the low- T structure; and $a = 7.963(2)$ Å and $V = 505.0(2)$ Å³ for the high- T structure ($R_p = 0.122$; $R_{wp} = 0.131$). The insets compare the relative line-broadening of the main peaks pre- and post-ball-milling. From the Scherrer equation, the particle size of the monoclinic-structured crystallites is estimated as 39 nm before ball-milling, decreasing to 13 nm after ball-milling.

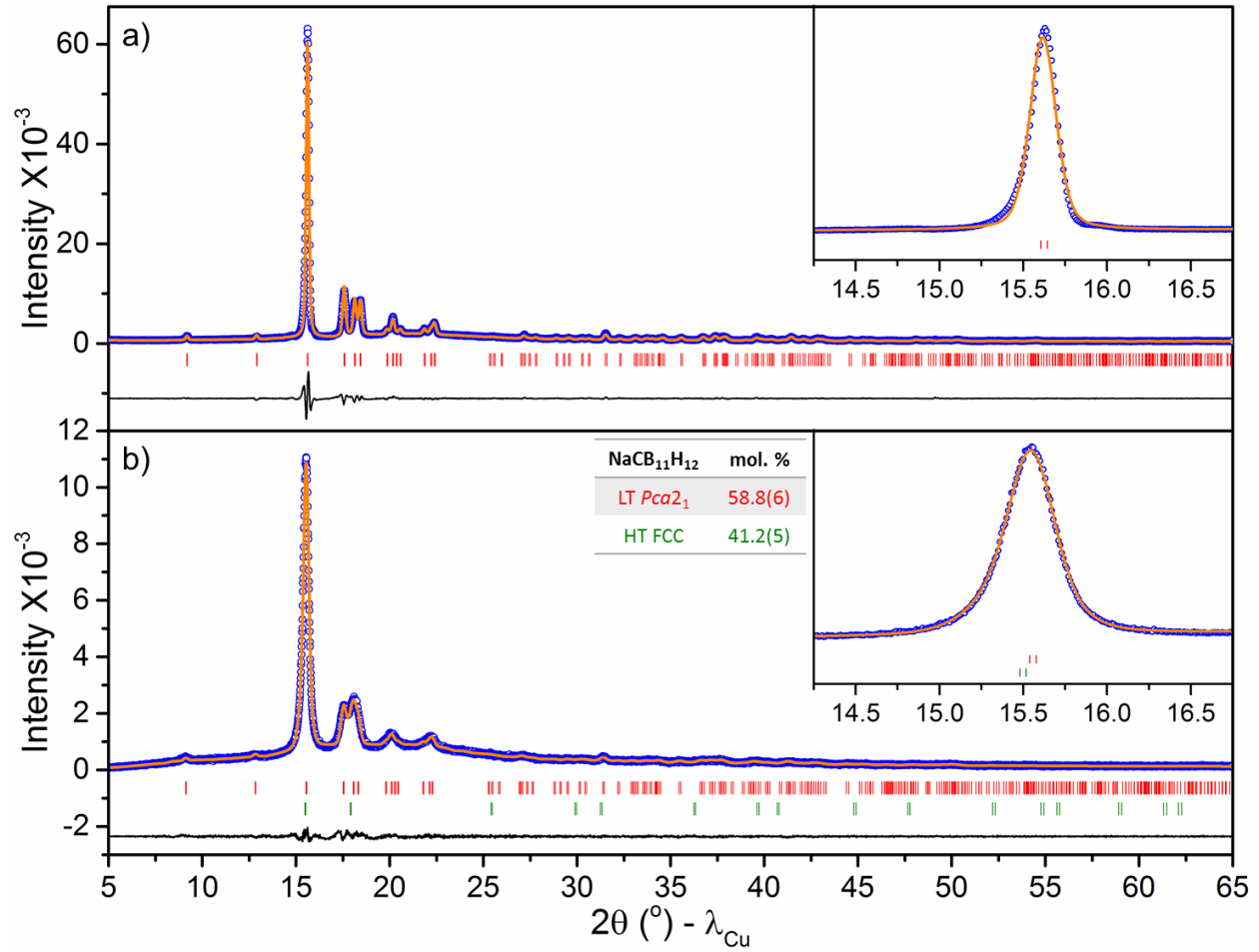


Figure S1. Room-*T* XRD data [experimental (blue circles), fitted (orange line), and difference (black line) patterns] for (a) pristine and (b) ball-milled NaCB₁₁H₁₂. Vertical red and green bars indicate the positions of Bragg peaks for the low-*T* (*Pca*2₁) orthorhombic and high-*T* (*Fm*-3*m*) face-centered-cubic (fcc) phases, respectively [4]. The refined unit cell parameters for the pristine sample are $a = 9.7821(4)$ Å, $b = 9.6254(4)$ Å, $c = 10.0928(4)$ Å, and $V = 950.30(6)$ Å³ for the low-*T* structure ($R_p = 0.091$; $R_{wp} = 0.093$). The refined unit cell parameters for the ball-milled sample are $a = 9.8192(6)$ Å, $b = 9.6868(5)$ Å, $c = 10.1159(5)$ Å, and $V = 962.18(9)$ Å³ for the low-*T* structure; and $a = 9.9065(5)$ Å and $V = 972.20(8)$ Å³ for the high-*T* structure ($R_p = 0.145$; $R_{wp} = 0.129$). The insets compare the relative line-broadening of the main peaks pre- and post-ball-milling. From the Scherrer equation, the particle size of the orthorhombic-structured crystallites is estimated as 44 nm before ball-milling, decreasing to 26 nm after ball-milling.

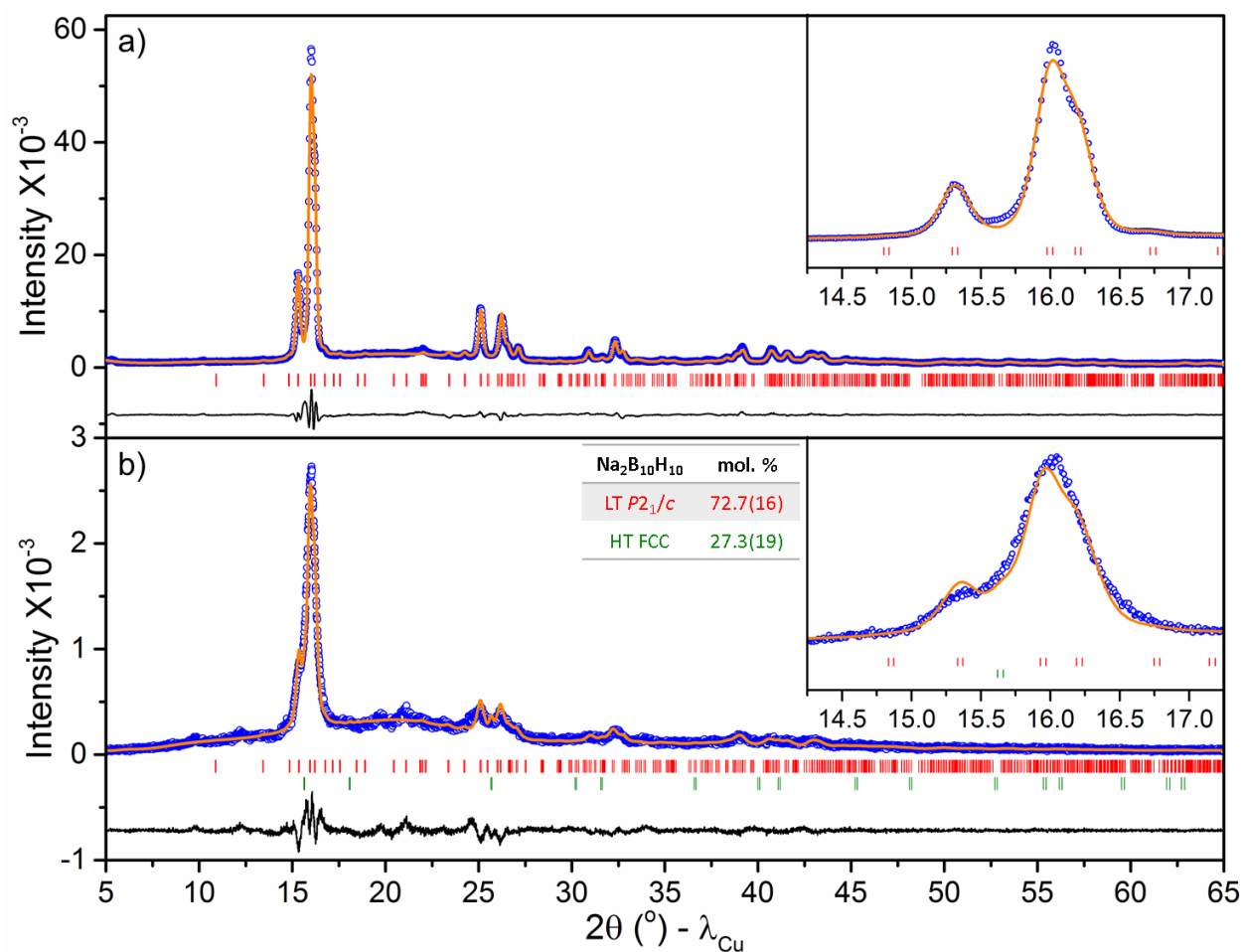


Figure S2. Room- T XRD data [experimental (blue circles), fitted (orange line), and difference (black line) patterns] for (a) pristine and (b) ball-milled $\text{Na}_2\text{B}_{10}\text{H}_{10}$. Vertical red and green bars indicate the positions of Bragg peaks for the low- T ($P2_1/c$) monoclinic and high- T ($Fm-3m$) fcc phases, respectively [5,6]. The refined unit cell parameters for the pristine sample are $a = 6.7263(4)$ Å, $b = 13.1520(8)$ Å, $c = 11.9671(6)$ Å, $\beta = 120.623(3)^\circ$, and $V = 911.02(9)$ Å³ for the low- T structure ($R_p = 0.127$; $R_{wp} = 0.134$). The refined unit cell parameters for the ball-milled sample are $a = 6.702(1)$ Å, $b = 13.189(3)$ Å, $c = 11.995(2)$ Å, $\beta = 120.508(9)^\circ$, and $V = 913.5(3)$ Å³ for the low- T structure; and $a = 9.817(2)$ Å and $V = 945.9(3)$ Å³ for the high- T structure ($R_p = 0.180$; $R_{wp} = 0.177$). The insets compare the relative line-broadening of the main peaks pre- and post-ball-milling. From the Scherrer equation, the particle size of the monoclinic-structured crystallites is estimated as 32 nm before ball-milling, decreasing to 23 nm after ball-milling.

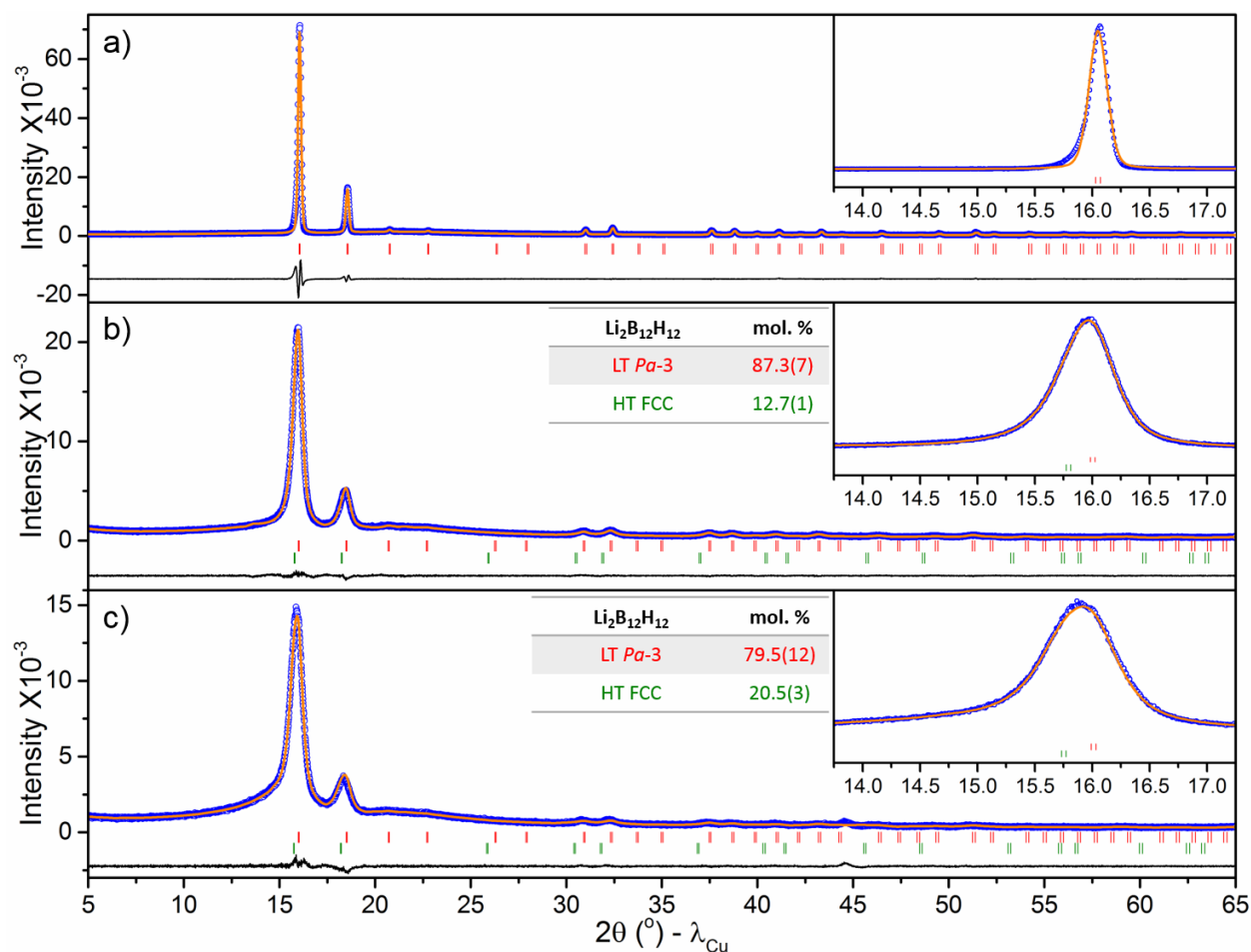


Figure S3. Room- T XRD data [experimental (blue circles), fitted (orange line), and difference (black line) patterns] for (a) pristine, (b) 16 h ball-milled, and (c) 80 h ball-milled $\text{Li}_2\text{B}_{12}\text{H}_{12}$. Vertical red and green bars indicate the positions of Bragg peaks for the low- T (*Pa*-3) cubic and high- T (*Fm*-3 m) fcc phases, respectively [2,7,8]. The refined unit cell parameters for the pristine sample are $a = 9.5678(2) \text{ \AA}$ and $V = 875.87(3) \text{ \AA}^3$ for the low- T structure ($R_p = 0.158$; $R_{wp} = 0.179$). The refined unit cell parameters for the 16 h ball-milled sample are $a = 9.5953(5) \text{ \AA}$ and $V = 883.45(8) \text{ \AA}^3$ for the low- T structure; and $a = 9.7230(9) \text{ \AA}$ and $V = 919.17(15) \text{ \AA}^3$ for the high- T structure ($R_p = 0.065$; $R_{wp} = 0.068$). The refined unit cell parameters for the 80 h ball-milled sample are $a = 9.5914(5) \text{ \AA}$ and $V = 882.36(8) \text{ \AA}^3$ for the low- T structure; and $a = 9.7482(7) \text{ \AA}$ and $V = 926.4(1) \text{ \AA}^3$ for the high- T structure ($R_p = 0.106$; $R_{wp} = 0.110$). The insets compare the relative line-broadening of the main peaks pre- and post-ball-milling. From the Scherrer equation, the particle size of the low- T -cubic-structured crystallites is estimated as 49 nm before ball-milling, decreasing to 15 nm after 16 h of ball-milling and 13 nm after 80 h of ball-milling.

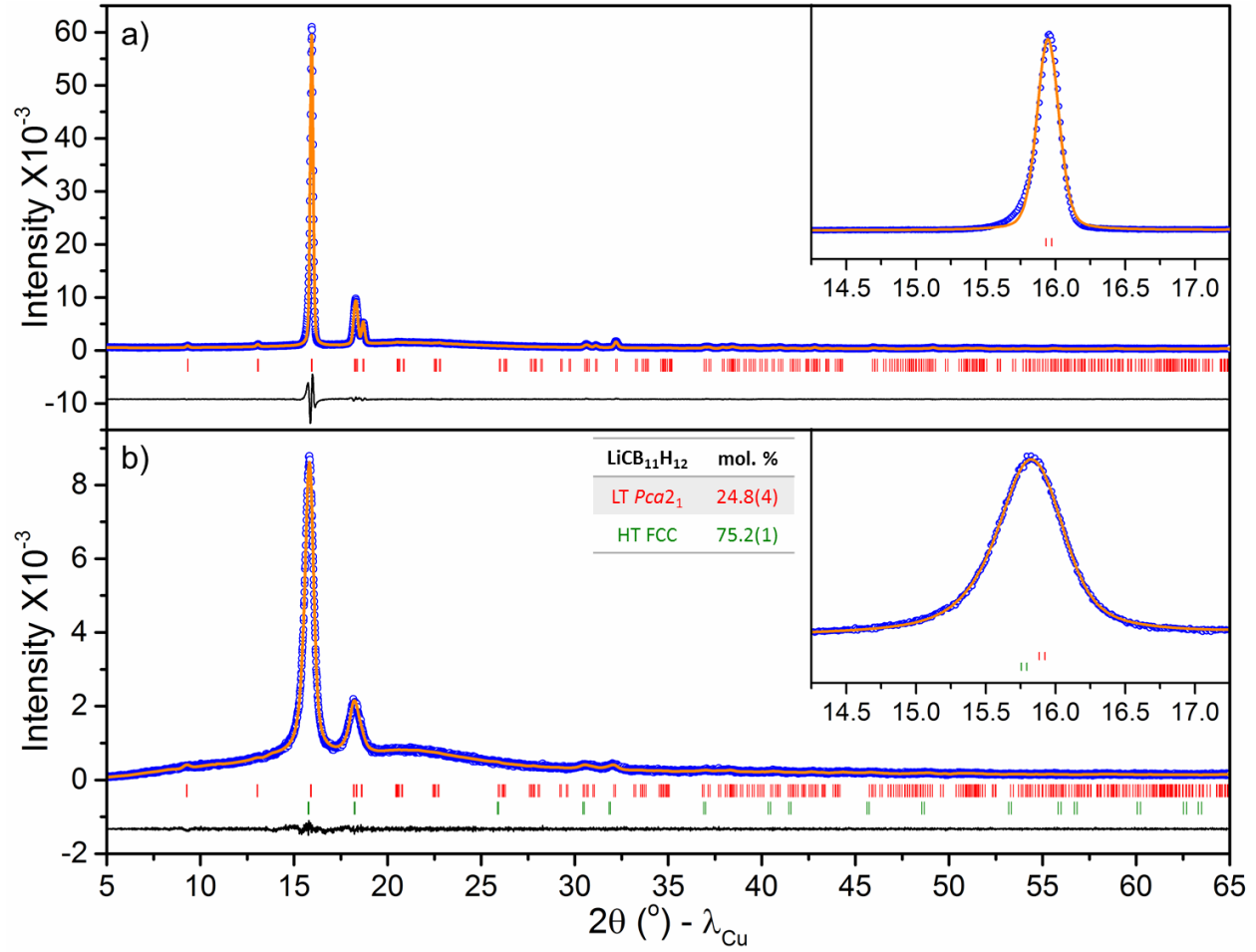


Figure S4. Room- T XRD data [experimental (blue circles), fitted (orange line), and difference (black line) patterns] for (a) pristine and (b) ball-milled $\text{LiCB}_{11}\text{H}_{12}$. Vertical red and green bars indicate the positions of Bragg peaks for the low- T ($Pca2_1$) orthorhombic and high- T ($Fm-3m$) fcc phases, respectively [4]. The refined unit cell parameters for the pristine sample are $a = 9.6668(5) \text{ \AA}$, $b = 9.4892(5) \text{ \AA}$, $c = 9.7273(5) \text{ \AA}$, and $V = 892.28(8) \text{ \AA}^3$ for the low- T structure ($R_p = 0.143$; $R_{wp} = 0.155$). The refined unit cell parameters for the ball-milled sample are $a = 9.678(1) \text{ \AA}$, $b = 9.537(1) \text{ \AA}$, $c = 9.7564(9) \text{ \AA}$, and $V = 900.5(2) \text{ \AA}^3$ for the low- T structure; and $a = 9.734(1) \text{ \AA}$ and $V = 922.4(2) \text{ \AA}^3$ for the high- T structure ($R_p = 0.105$; $R_{wp} = 0.106$). The insets compare the relative line-broadening of the main peaks pre- and post-ball-milling. From the Scherrer equation, the particle size of the orthorhombic-structured crystallites is estimated as 45 nm before ball-milling, decreasing to 15 nm after ball-milling.

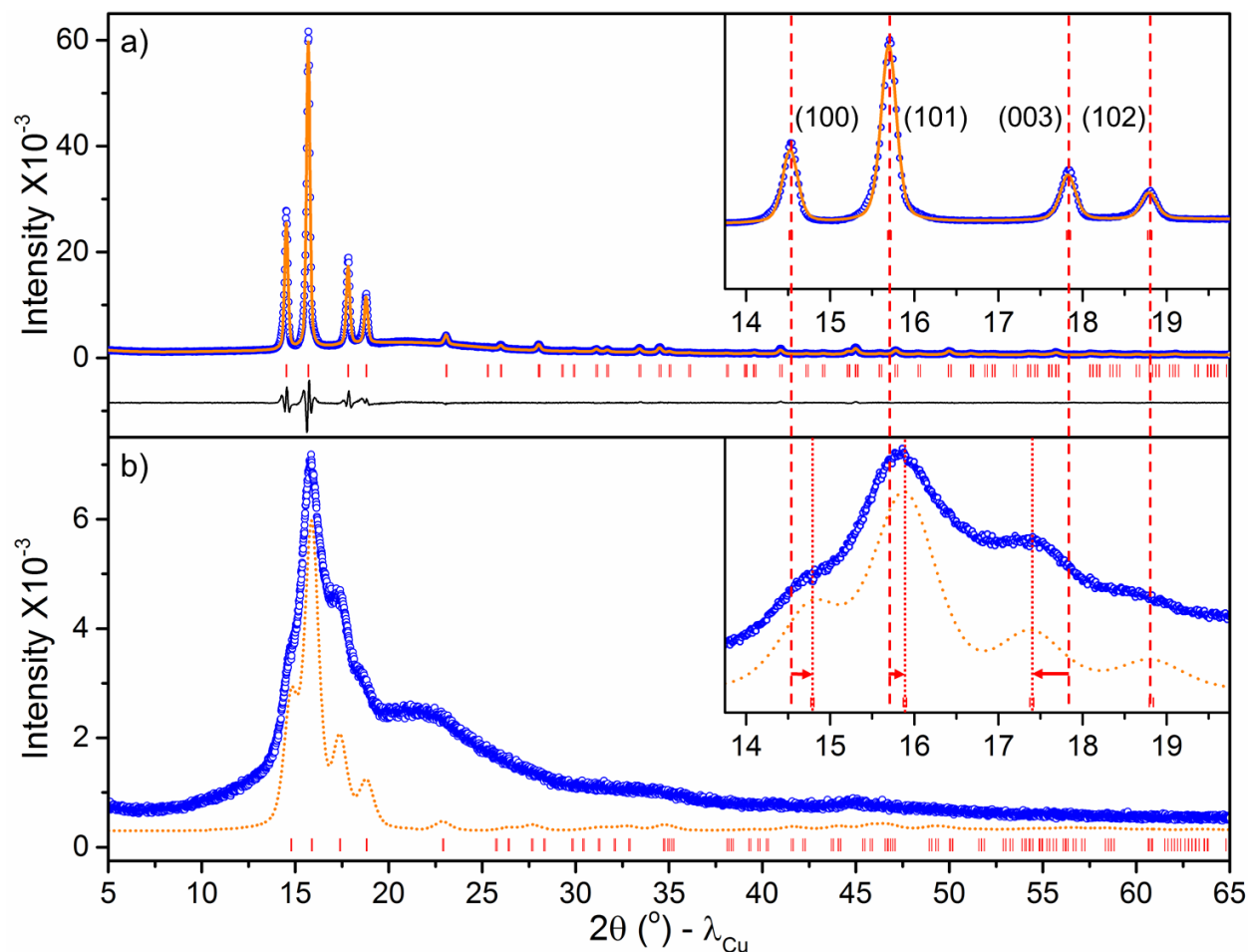


Figure S5. Room-*T* XRD patterns for (a) pristine and (b) ball-milled $\text{Li}_2\text{B}_{10}\text{H}_{10}$. Experimental (blue circles), fitted (orange line) and difference (black line) are shown for the pristine sample. Vertical red bars indicate the positions of Bragg peaks for the low-*T* ($P6_422$) hexagonal phase [9]. There is clearly disorder present in the ball-milled material, although its structure is still not established. The refined unit cell parameters for the pristine sample are $a = 7.0416(4)$ Å, $c = 14.9266(7)$ Å, and $V = 640.97(6)$ Å³ for the low-*T* structure ($R_p = 0.140$; $R_{wp} = 0.141$). The significant peak broadening, amorphous background, and unknown structure of the high-*T*-disordered phase prevents any analysis by Rietveld refinement. The generated pattern (orange dotted line) for the ball-milled sample (for a possible hexagonal disordered phase) is based on the low-*T* hexagonal structure, but with modified unit cell parameters of $a = 6.92$ Å, $c = 15.30$ Å, and $V = 634.5$ Å³. The significant expansion along the *c*-direction would be consistent with the space needed to accommodate fully orientationally disordered $\text{B}_{10}\text{H}_{10}^{2-}$ anions. The insets compare the relative line-broadening of the main peaks pre- and post-ball-milling. After ball-milling, the positions of the four main Bragg peaks are shifted as seen from the red dashed line (pristine) to the red dotted line (after ball-milling).

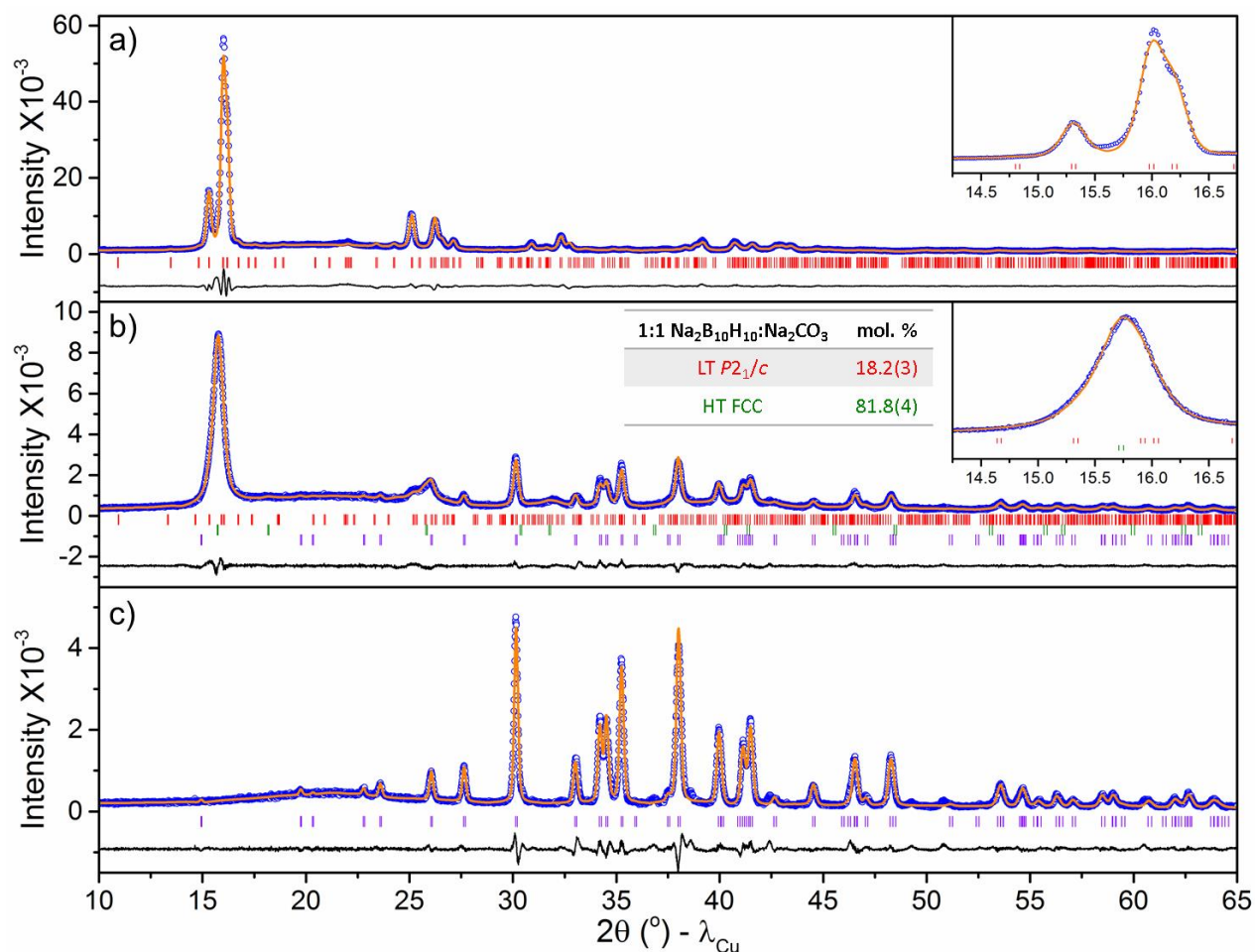


Figure S6. Room-*T* XRD data [experimental (blue circles), fitted (orange line), and difference (black line) patterns] for (a) pristine Na₂B₁₀H₁₀, (b) ball-milled 1:1 Na₂B₁₀H₁₀:Na₂CO₃, and (c) pristine Na₂CO₃. Vertical red and green bars indicate the positions of Bragg peaks for the low-*T* (*P*2₁/*c*) monoclinic and high-*T* (*Fm*-3*m*) fcc Na₂B₁₀H₁₀ phases, respectively; purple bars indicate those for (*C*2/*m*) monoclinic Na₂CO₃ [10]. The refined unit cell parameters for the pristine Na₂B₁₀H₁₀ sample are $a = 6.7263(4)$ Å, $b = 13.1520(8)$ Å, $c = 11.9671(6)$ Å, $\beta = 120.623(3)^\circ$, and $V = 911.02(9)$ Å³ for the low-*T* structure ($R_p = 0.127$; $R_{wp} = 0.134$) (cf. Fig. S2a). The refined unit cell parameters for the ball-milled 1:1 Na₂B₁₀H₁₀:Na₂CO₃ sample are $a = 6.795(2)$ Å, $b = 13.294(4)$ Å, $c = 11.988(4)$ Å, $\beta = 121.70(2)^\circ$, and $V = 921.4(5)$ Å³ for the low-*T* Na₂B₁₀H₁₀ structure; $a = 9.7608(3)$ Å and $V = 929.94(5)$ Å³ for the high-*T* Na₂B₁₀H₁₀ structure; and $a = 8.9101(2)$ Å, $b = 5.2413(1)$ Å, $c = 6.0461(1)$, and $\beta = 101.304(2)^\circ$ for Na₂CO₃ ($R_p = 0.115$; $R_{wp} = 0.116$). The refined unit cell parameters for the pristine Na₂CO₃ sample are $a = 8.9114(2)$ Å, $b = 5.2423(1)$ Å, $c = 6.0454(2)$, and $\beta = 101.339(1)^\circ$ ($R_p = 0.162$; $R_{wp} = 0.179$). The insets compare the relative line-broadening of the main peaks pre- and post-ball-milling. From the Scherrer equation, the particle size of the monoclinic-structured Na₂B₁₀H₁₀ crystallites is estimated as 32 nm before ball-milling, decreasing to 21 nm after ball-milling.

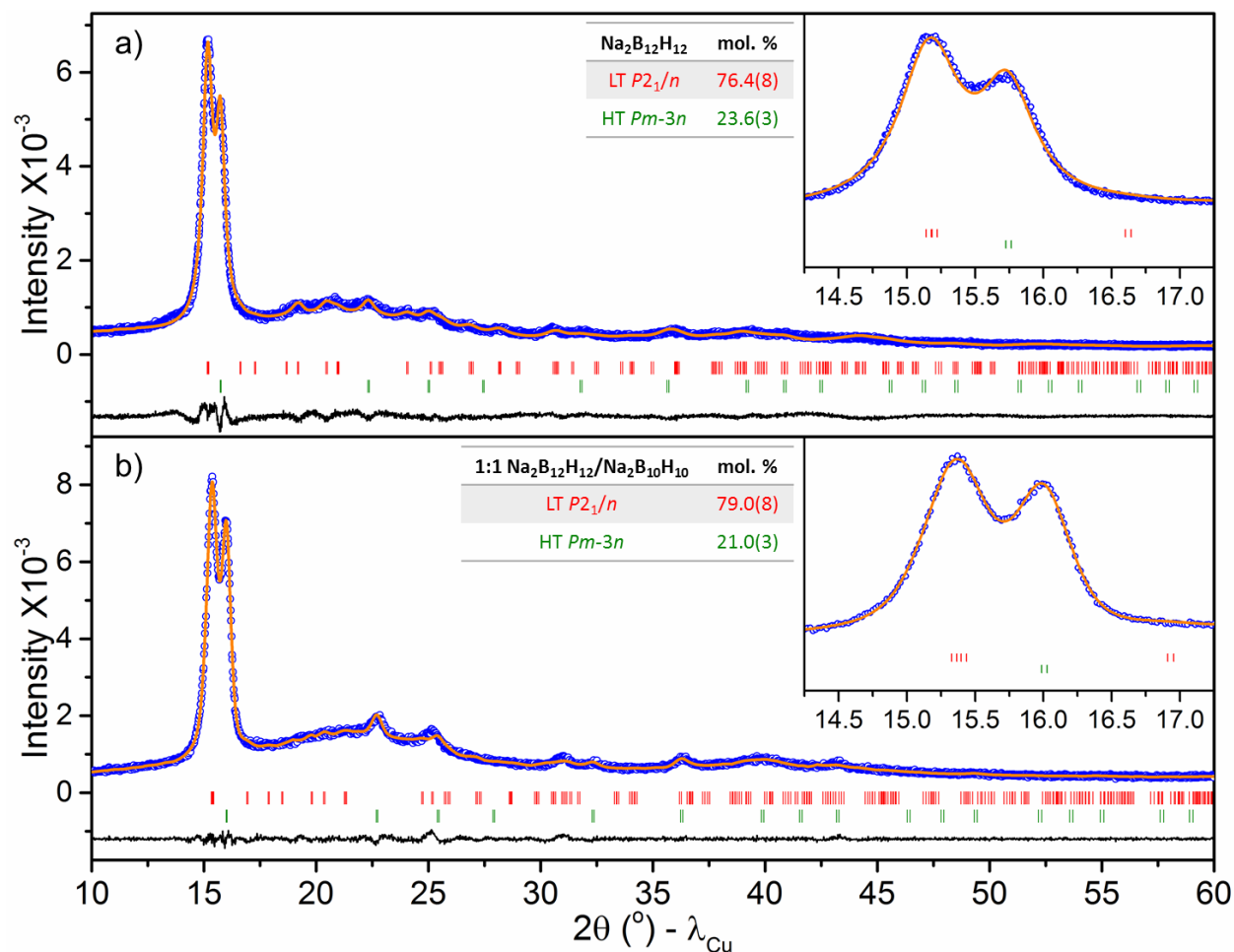


Figure S7. Room- T XRD data [experimental (blue circles), fitted (orange line), and difference (black line) patterns] for (a) ball-milled $\text{Na}_2\text{B}_{12}\text{H}_{12}$ and (b) a 1:1 $\text{Na}_2\text{B}_{12}\text{H}_{12}:\text{Na}_2\text{B}_{10}\text{H}_{10}$ mixture ball-milled for 3.2 h followed by vacuum annealing at 548 K for 16 h. Vertical red and green bars indicate the positions of Bragg peaks for the low- T ($P2_1/n$) monoclinic and high- T ($Pm-3n$) pseudo-bcc phases, respectively. The similarity of the mixed-compound pattern to that for $\text{Na}_2\text{B}_{12}\text{H}_{12}$ strongly suggests the presence of similar ordered monoclinic and disordered bcc solid-solution phases for the mixed compound (each containing both $\text{B}_{12}\text{H}_{12}^{2-}$ and $\text{B}_{10}\text{H}_{10}^{2-}$ anions), but with slightly smaller lattice constants than for pure $\text{Na}_2\text{B}_{12}\text{H}_{12}$. The refined unit cell parameters for the ball-milled $\text{Na}_2\text{B}_{12}\text{H}_{12}$ sample are $a = 6.981(2)$ Å, $b = 10.672(3)$ Å, $c = 7.009(3)$ Å, $\beta = 94.40(2)^\circ$, and $V = 520.7(3)$ Å³ for the low- T structure; and $a = 7.9634(19)$ Å and $V = 505.0(2)$ Å³ for the high- T structure ($R_p = 0.122$; $R_{wp} = 0.131$) (cf. Fig. 1b). Assuming similar low- T and high- T $\text{Na}_2\text{B}_{12}\text{H}_{12}$ structures but with average B and H site occupancies of 11/12, the refined unit cell parameters for the ball-milled $\text{Na}_2\text{B}_{12}\text{H}_{12}:\text{Na}_2\text{B}_{10}\text{H}_{10}$ sample are $a = 6.882(3)$ Å, $b = 10.477(5)$ Å, $c = 6.927(3)$ Å, $\beta = 91.9(3)^\circ$, and $V = 499.1(4)$ Å³ for the low- T structure; and $a = 7.8333(1)$ Å and $V = 480.6(2)$ Å³ for the high- T structure ($R_p = 0.112$; $R_{wp} = 0.098$). These cell volumes are intermediate between those for $\text{Na}_2\text{B}_{12}\text{H}_{12}$ and $\text{Na}_2\text{B}_{10}\text{H}_{10}$, which is consistent with the formation of a solid-solution mixed-anion phase.

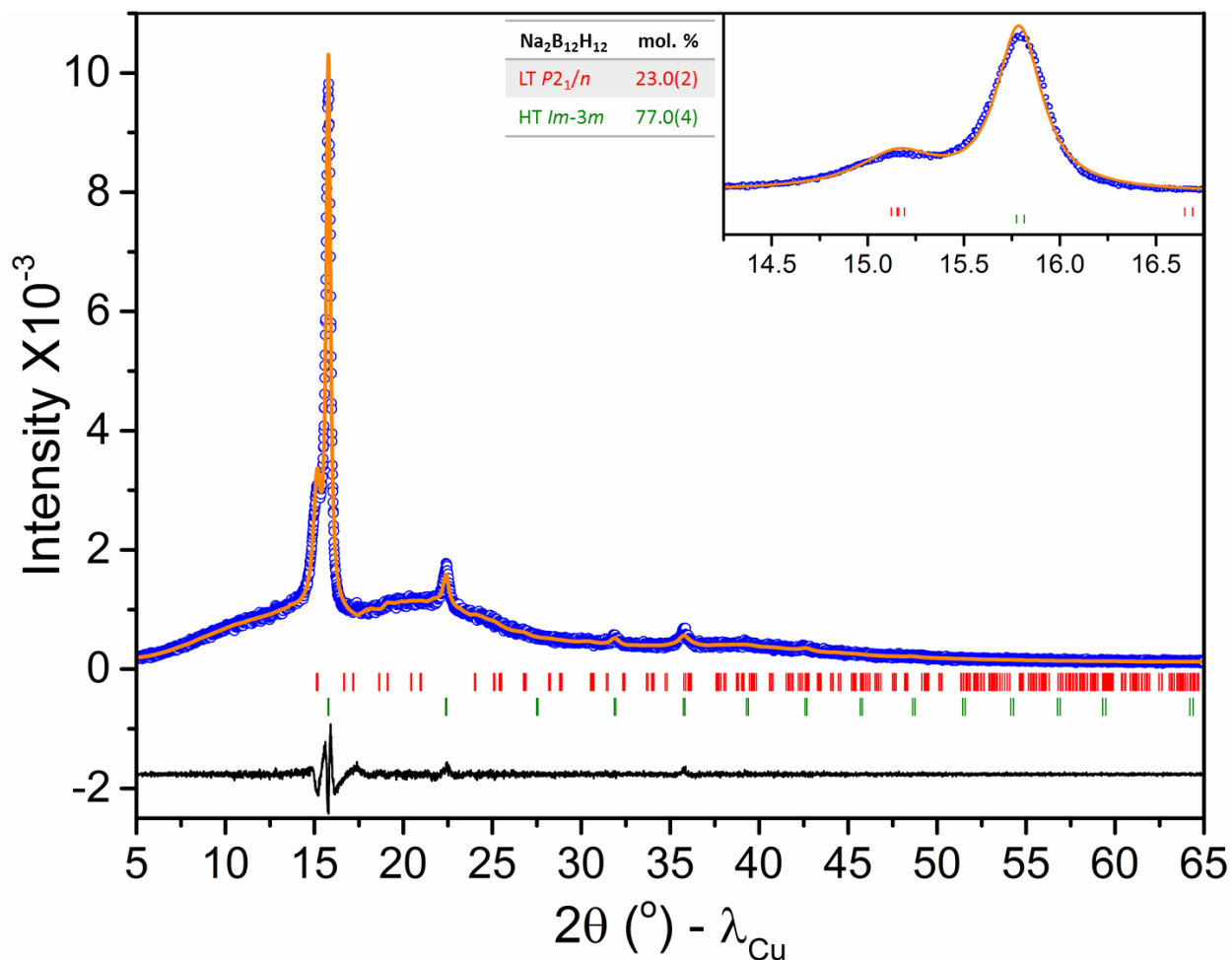


Figure S8. Room- T XRD data [experimental (blue circles), fitted (orange line), and difference (black line) patterns] for ball-milled $\text{Na}_2\text{B}_{12}\text{H}_{12}$ after annealing at 620 K for 13 d. Vertical red and green bars indicate the positions of Bragg peaks for the low- T ($P2_1/n$) monoclinic and high- T ($Im-3m$) bcc phases, respectively. The fully disordered $Im-3m$ bcc structure [2] (instead of the intermediate pseudo-bcc $Pm-3n$ structure) indexed best with the observed pattern. The refined unit cell parameters are $a = 7.033(5)$ Å, $b = 10.641(6)$ Å, $c = 7.013(3)$ Å, $\beta = 94.61(5)^\circ$, and $V = 523.1(5)$ Å³ for the low- T monoclinic structure; and $a = 7.938(2)$ Å and $V = 500.3(2)$ Å³ for the high- T bcc structure ($R_p = 0.177$; $R_{wp} = 0.154$). As shown by the NPD data in Fig. S9, this indicates that the stabilized bcc phase for $\text{Na}_2\text{B}_{12}\text{H}_{12}$ increases upon annealing, even at 620 K, and is surprisingly robust with respect to temperature. Although not evaluated under these treatment conditions, it is likely that the ionic conductivity will be further enhanced with respect to that in Fig. 3.

Neutron Powder Diffraction (NPD) Measurements

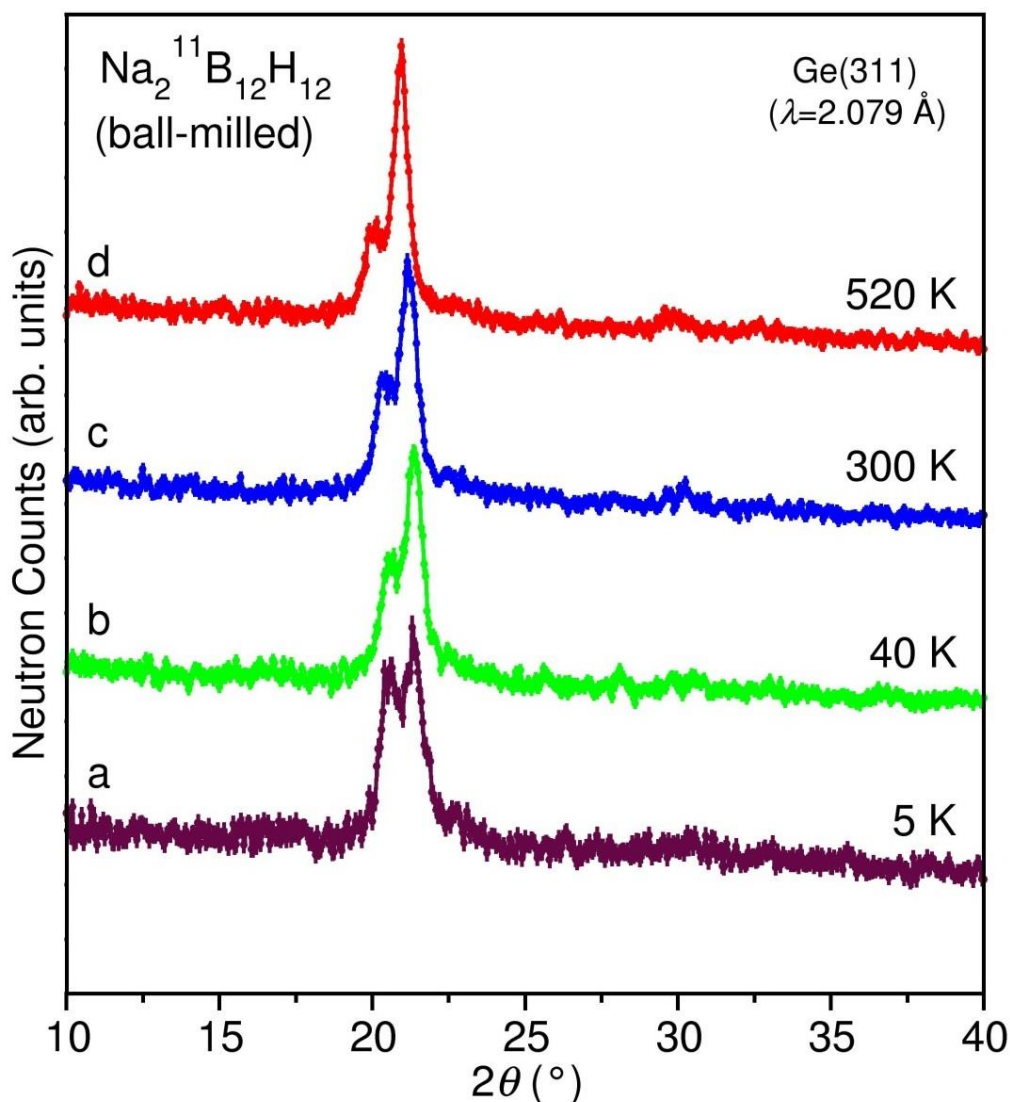


Figure S9. NPD patterns [BT-1 Powder Diffractometer, Ge(311) mono., $\lambda=2.079 \text{ \AA}$] for $\text{Na}_2^{11}\text{B}_{12}\text{H}_{12}$: (a) at 5 K after ball-milling for 72 h and annealing at 410 K for 12 h. The bimodal feature represents the Bragg scattering from the ordered monoclinic (at lower angle) and disordered bcc (at higher angle) phases. Fig. S10 compares the 4 K neutron vibrational spectrum for this material at this thermal treatment stage with that for pristine $\text{Na}_2^{11}\text{B}_{12}\text{H}_{12}$. Subsequently, the neutron fixed-window scans (FWSs) and QENS data in Fig. 2 were collected up to 520 K. More NPD patterns were then collected at (b) 40 K, (c) 300 K, and (c) 520 K, indicating an increased bcc-phase fraction compared to (a) and an increasing bcc-phase fraction with temperature, in line with the FWS behavior in Fig. 2. The conductivity data in Fig. 3 was finally collected at this stage.

Neutron Vibrational Spectroscopy (NVS) Measurements

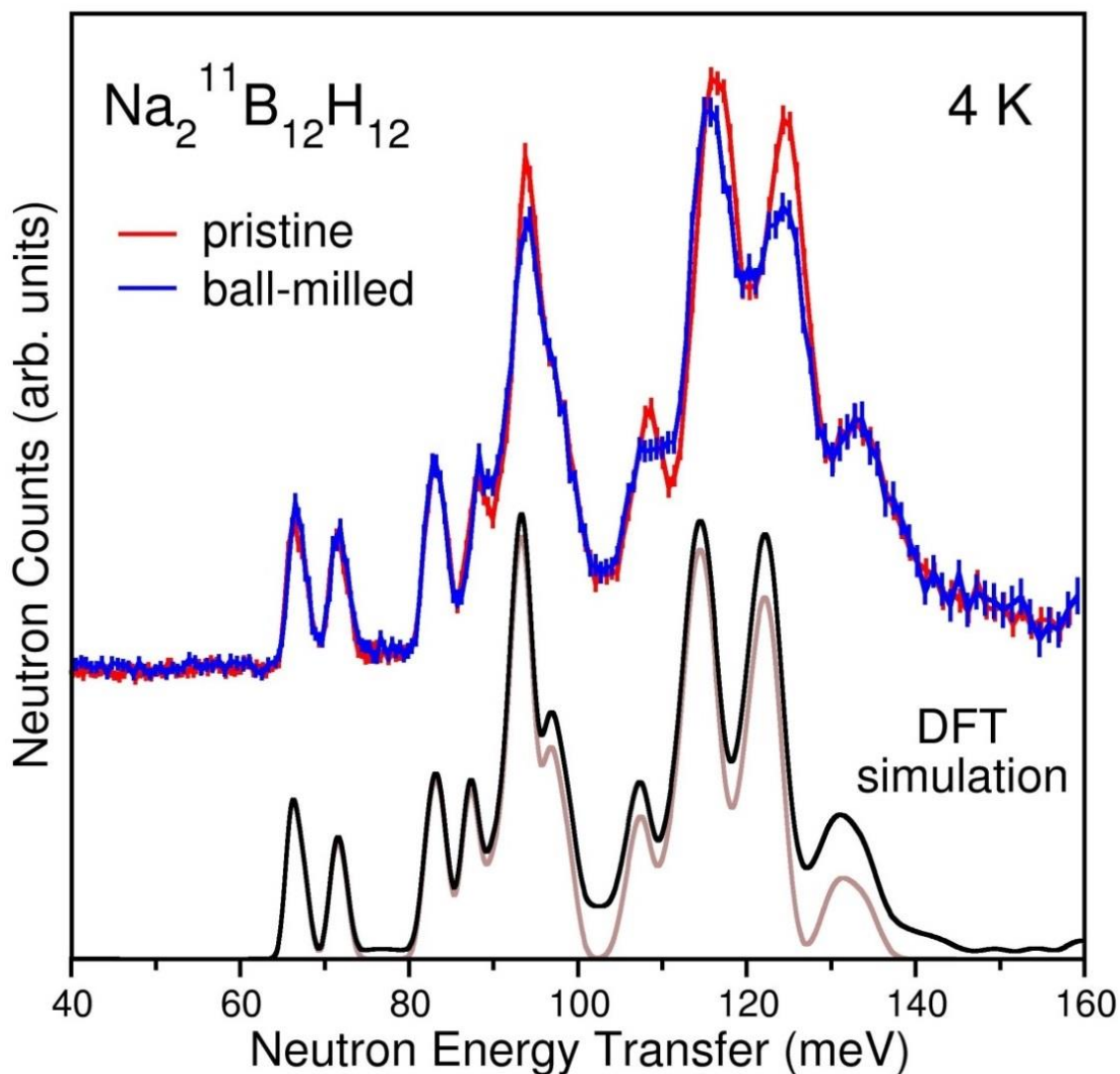


Figure S10. Neutron vibrational spectra at 4 K of $\text{Na}_2^{11}\text{B}_{12}\text{H}_{12}$ before and after ball-milling for 72 h and annealing at 410 K for 12 h (using the Filter-Analyzer Neutron Spectrometer [11] with the Cu(220) monochromator) compared to the simulated one-phonon (brown) and one+two-phonon (black) densities of states from DFT phonon calculations [3] of the optimized ordered monoclinic structure. (N.B., $1 \text{ meV} \approx 8.066 \text{ cm}^{-1}$.) The disordered ball-milled sample displays some minor but clear perturbations of some anion internal-vibration bands compared to pristine monoclinic $\text{Na}_2^{11}\text{B}_{12}\text{H}_{12}$.

Scanning Electron Microscopy (SEM) Measurements

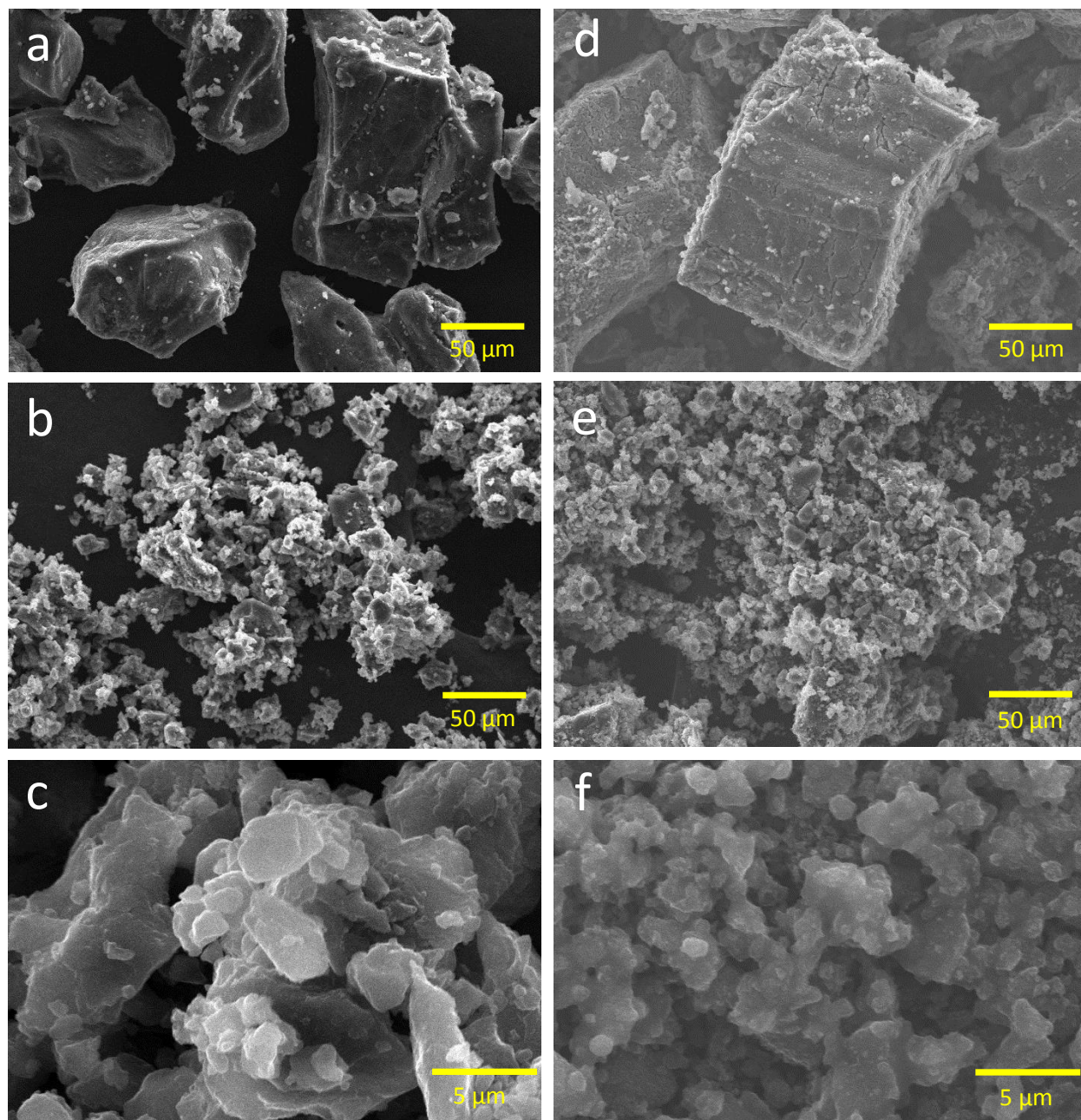


Figure S11. SEM images (using the JEOL JSM6009) of (a) pristine $\text{Na}_2\text{B}_{12}\text{H}_{12}$, (b) and (c) 72 h ball-milled $\text{Na}_2\text{B}_{12}\text{H}_{12}$ from the text, (d) pristine $\text{Li}_2\text{B}_{12}\text{H}_{12}$, and (e) and (f) 20 h ball-milled $\text{Li}_2\text{B}_{12}\text{H}_{12}$ from Fig. S15. After ball-milling, the particle size decreases to a few microns from 100-200 μm , and agglomeration occurs, as is often characteristic for the method.

Differential Scanning Calorimetry (DSC) Measurements

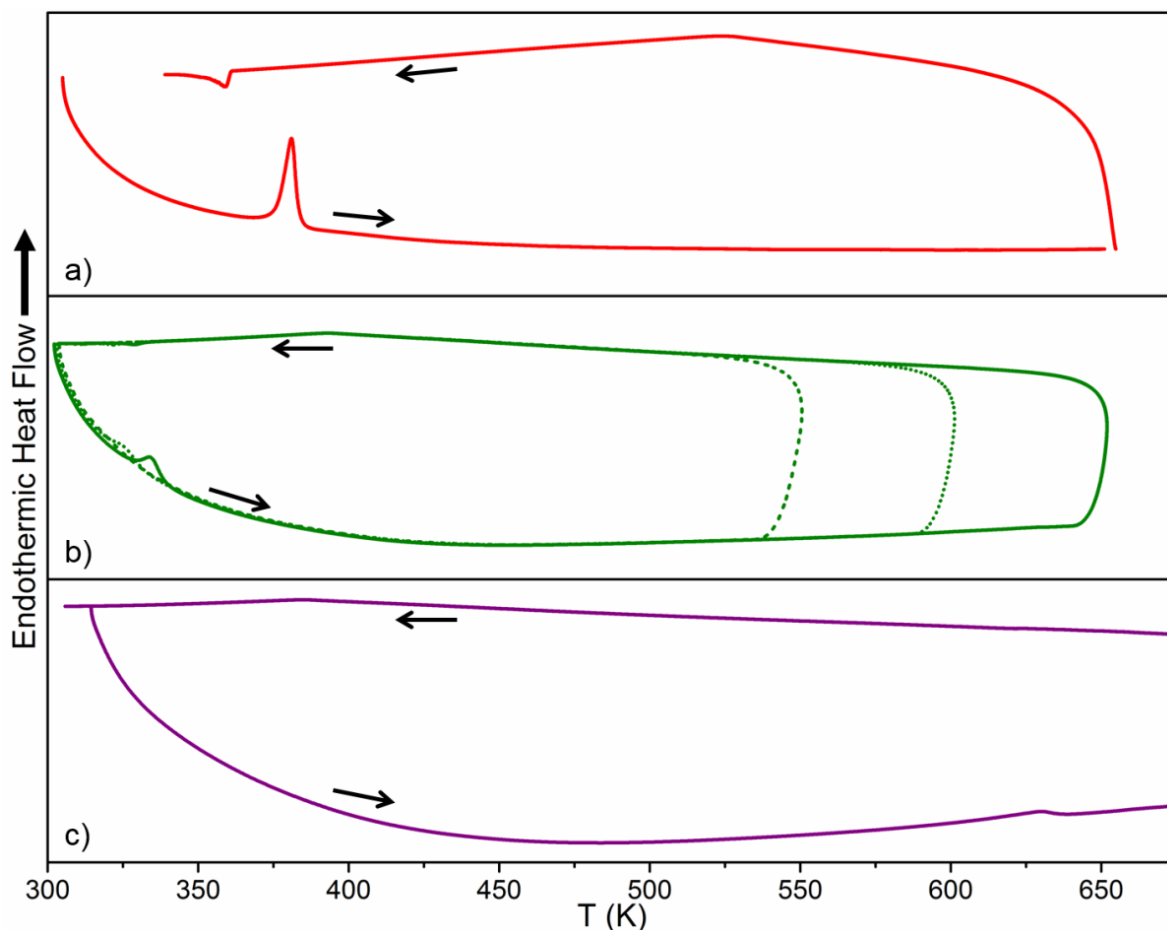


Figure S12. DSC measurements for (a) pristine $\text{Na}_2\text{B}_{10}\text{H}_{10}$, (b) a 1:1 $\text{Na}_2\text{B}_{10}\text{H}_{10}:\text{Na}_2\text{CO}_3$ mixture ball-milled for 28 h (first cycle up to 550 K, dashed line; second cycle up to 600 K, dotted line; third cycle up to 650 K, solid line) and (c) pristine Na_2CO_3 . Measurements were made with a Netzsch (STA 449 F1 Jupiter) TGA-DSC under He flow with Al sample pans. Heating rates were 5 K min^{-1} ; cooling rates below 375 K were less than 2 K min^{-1} . There is no order-disorder phase transition evident for the ball-milled mixture during the first 550 K cycle. The second (600 K) cycle shows the emergence of a transition peak, which shifts upward and narrows during the third cycle (650 K). The appearance of the transition peak with increasing maximum cycle temperature is presumably due to increased particle sizes and reduced defects through accelerated sintering of this material. Even so, the resulting T_{trans} values after annealing the ball-milled mixture are still much lower than for pristine $\text{Na}_2\text{B}_{10}\text{H}_{10}$.

AC Impedance/Cyclic Voltammetry Measurements

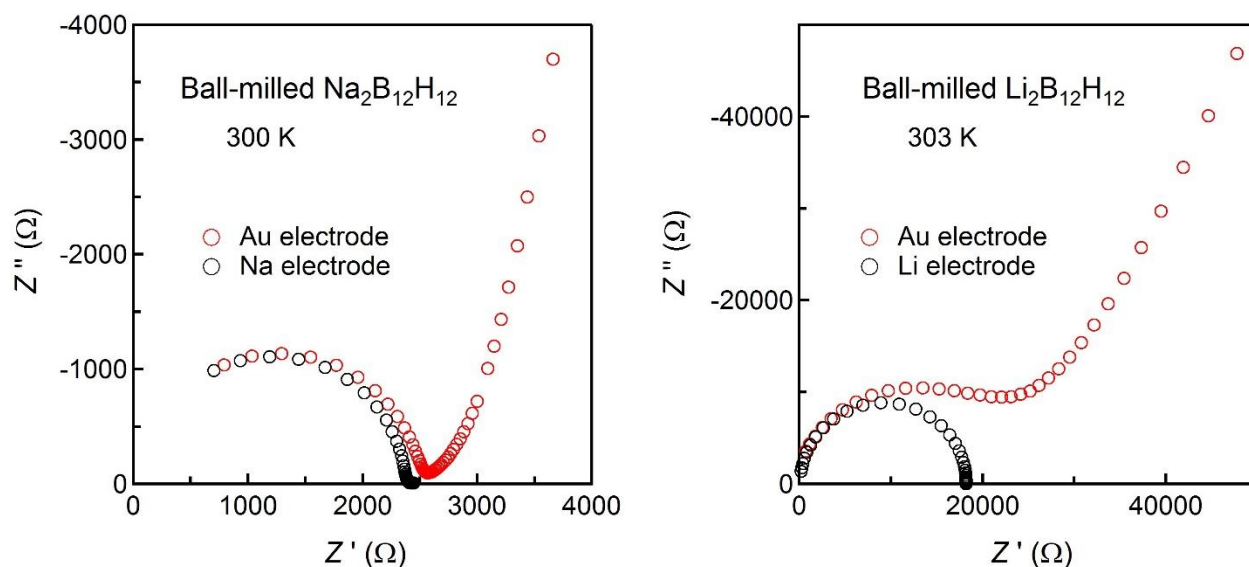


Figure S13. Symmetric-cell complex-impedance plots for ball-milled Na₂B₁₂H₁₂ and Li₂B₁₂H₁₂. The electrodes were mechanically fixed onto both pellet faces. The Na-symmetric-cell spectrum for ball-milled Na₂B₁₂H₁₂ consists of only a semi-circle due to contributions from the bulk and grain boundaries. On the other hand, for a Au-symmetric cell, a spike appears after the semi-circle in the low-frequency region caused by the electrode contribution. Similar behavior is observed for ball-milled Li₂B₁₂H₁₂ upon comparison of Li-symmetric and Au-symmetric cells.

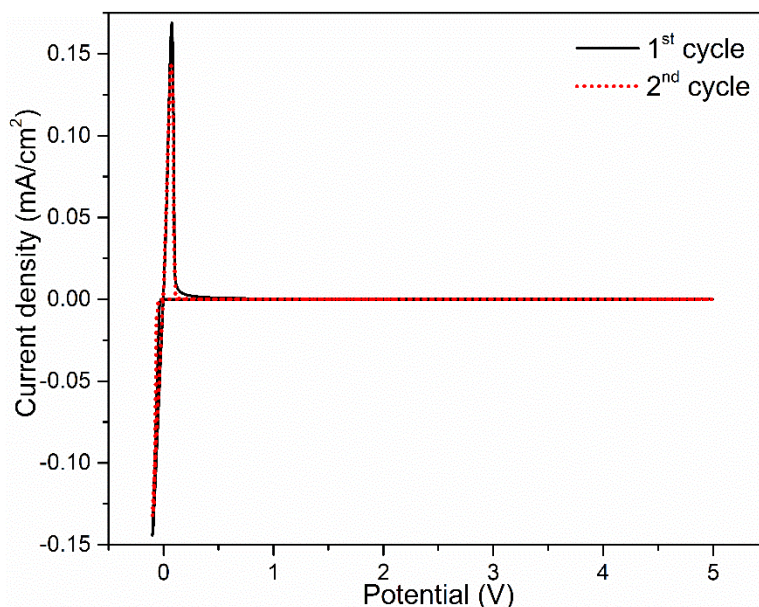


Figure S14. Cyclic voltammetry data (at 5 mV/s) for ball-milled Na₂B₁₂H₁₂ sandwiched by Na and Mo electrodes at 303 K using a potentiostat/galvanostat (Princeton VersaSTAT4). Reversible Na deposition/stripping was observed nearly at 0 V, and no irreversible oxidation current appeared up to 5 V.

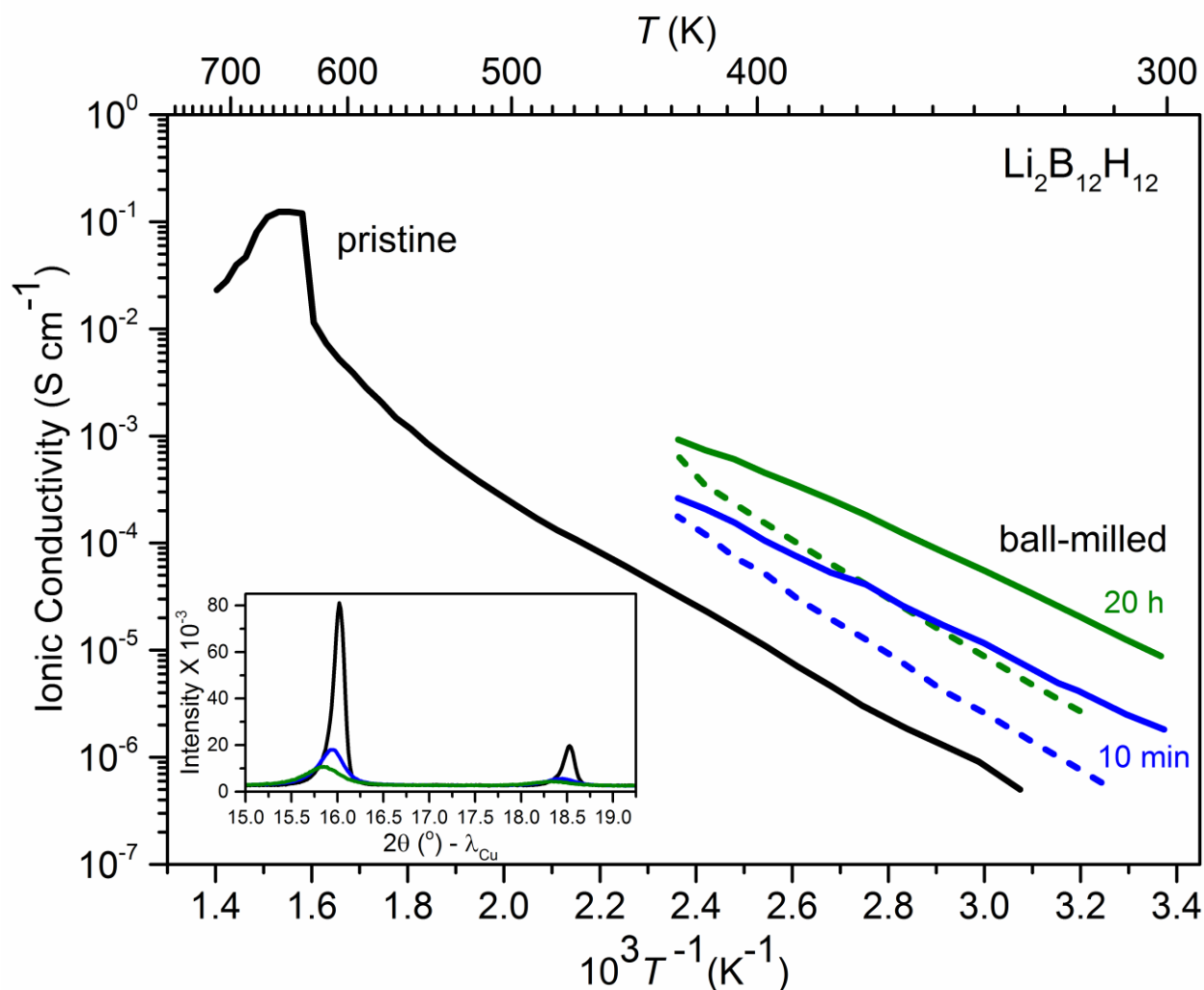


Figure S15. Comparative ionic conductivity plots for $\text{Li}_2\text{B}_{12}\text{H}_{12}$ vs. $1/T$ before (black) and after ball-milling for 10 min (blue) and 20 h (green). (N.B., this is a different $\text{Li}_2\text{B}_{12}\text{H}_{12}$ sample than shown in Fig. S3; corresponding XRD patterns in the inset again show evidence of increasing fraction of disordered phase with increasing ball-milling time, as in Fig S3). Solid lines denote the 1st heating runs. Dashed lines denote the 4th heating runs. Conductivities increase with ball-milling time. Reduced conductivities after repeated cycling to 413 K reflect the slow reversion back towards the original sample morphology. The conductivity decay of the pristine sample with increasing temperature above the 615 K order-disorder phase transition reflects the expected decomposition of the material at these temperatures. It is evident that the initial 10 min of ball-milling already generates enough superionic phase to increase the conductivity by an order of magnitude. Also, unlike for $\text{Na}_2\text{B}_{12}\text{H}_{12}$, it is clear that staying some distance below 413 K is required to inhibit $\text{Li}_2\text{B}_{12}\text{H}_{12}$ morphological reversion after ball-milling.

References

- [1] A.L. Patterson, *Phys. Rev.* 56 (1939) 978–982.
- [2] N. Verdal, J.-H. Her, V. Stavila, A.V. Soloninin, O.A. Babanova, A.V. Skripov, T.J. Udovic, J.J. Rush, *J. Solid State Chem.* 212 (2014) 81–91.
- [3] J.-H. Her, W. Zhou, V. Stavila, C.M. Brown, T.J. Udovic, *J. Phys. Chem. C* 113 (2009) 11187–11189.
- [4] W.S. Tang, A. Unemoto, W. Zhou, V. Stavila, M. Matsuo, H. Wu, S. Orimo, T.J. Udovic, *Energy Environ. Sci.* 8 (2015) 3637–3645.
- [5] T.J. Udovic, M. Matsuo, W.S. Tang, H. Wu, V. Stavila, A.V. Soloninin, R.V. Skoryunov, O.A. Babanova, A.V. Skripov, J.J. Rush, A. Unemoto, H. Takamura, S. Orimo, *Adv. Mater.* 26 (2014) 7622–7626.
- [6] H. Wu, W.S. Tang, W. Zhou, V. Stavila, J.J. Rush, T.J. Udovic, *CrystEngComm* 17 (2015) 3533–3540.
- [7] J.-H. Her, M. Yousufuddin, W. Zhou, S.S. Jalisatgi, J.G. Kulleck, J.A. Zan, S.-J. Hwang, R.C. Bowman, Jr., T.J. Udovic, *Inorg. Chem.* 47 (2008) 9757–9759.
- [8] M. Paskevicius, M.P. Pitt, D.H. Brown, D.A. Sheppard, S. Chumphongphan, C.E. Buckley, *Phys. Chem. Chem. Phys.* 15 (2013) 15825–15828.
- [9] H. Wu, W.S. Tang, V. Stavila, W. Zhou, J.J. Rush, T.J. Udovic, *J. Phys. Chem. C* 119 (2015) 6481–6487.
- [10] I. P. Swainson, M. T. Dove and M. J. Harris, *J. Phys.: Condens. Matter*, 1995, 7, 4395–4417.
- [11] T.J. Udovic, C.M. Brown, J.B. Leão, P.C. Brand, R.D. Jiggetts, R. Zeitoun, T.A. Pierce, I. Peral, J.R.D. Copley, Q. Huang, D.A. Neumann, R.J. Fields, *Nucl. Instr. Meth. A* 588 (2008) 406–413.